Earth, Planets and Space

FULL PAPER

Open Access

Linking the spatiotemporal distribution of static stress drops to source faults in a fluid-driven earthquake swarm, northeastern Noto Peninsula, central Japan

Mitsuteru Fukuoka[1], Yoshihiro Hiramatsu[2*] and Takuji Yamada[3]

Abstract

We investigated stress drops during an earthquake swarm in northeastern Noto Peninsula, central Japan, which is characterized by ongoing seismic activity in four clusters. We focused on the spatiotemporal distribution of the static stress drop and its relationship with the source faults of the earthquake swarm. Employing the empirical Green's function method, we estimated static stress drops for 90 earthquakes of M_{JMA} 3.0–5.4. We obtained logarithmic mean stress drops of 13 MPa and 19 MPa from P-wave and S-wave analyses, respectively, which were typical values for crustal earthquakes. We comprehensively analyzed the spatiotemporal distribution of static stress drops in the northern cluster due to the abundance of available data and clarity of fault structures there. We observed larger static stress drops for earthquakes along shallow portions of the source faults, as defined by the hypocentral distribution during a given period. Conversely, we observed smaller static stress drops for earthquakes at medial parts along the faults. These results suggest higher fault strength at shallower parts along the faults and reduced fault strength at medial parts. We attribute the high fault strength at shallow parts to low pore fluid pressure after only limited fluid diffusion near the fault terminus. In contrast, we attribute the reduction in fault strength at medial parts to high pore fluid pressure within the fault following penetration by migrating fluids.

Keywords Diffusion, Pore fluid pressure, Fault strength, Empirical Green's function, Static stress drop, Earthquake swarm

*Correspondence:
Yoshihiro Hiramatsu
yoshizo@staff.kanazawa-u.ac.jp
Full list of author information is available at the end of the article

Graphical Abstract

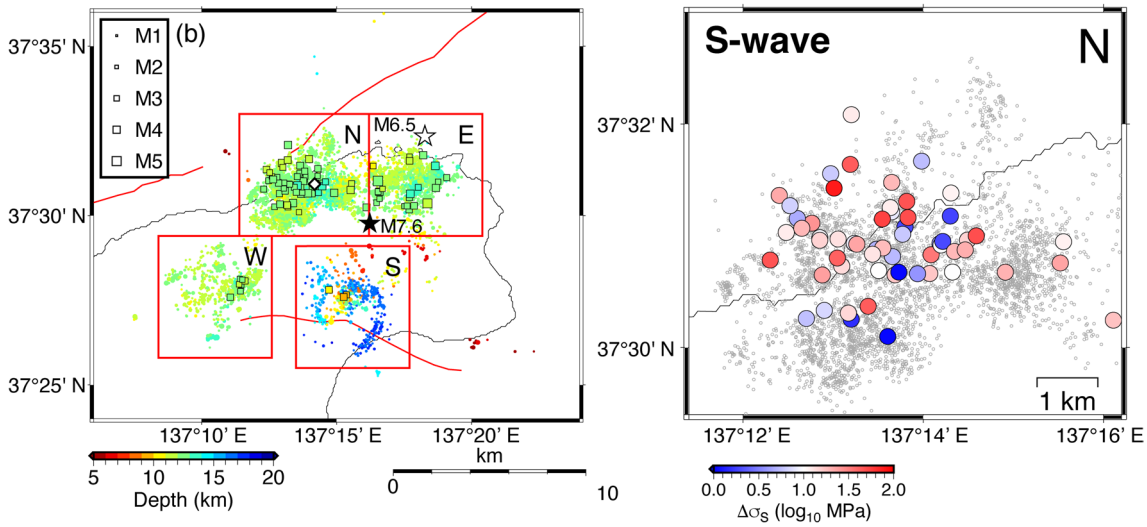

1 Introduction

The static stress drop during an earthquake represents the difference between the initial and residual stresses on a fault before and after a rupture, respectively. This parameter is fundamental for elucidating the rupture dynamics of an earthquake. Previous studies have demonstrated that static stress drops are nearly constant over a wide range of earthquake magnitudes (e.g., Abercrombie 1995; Hiramatsu et al. 2002; Imanishi and Ellsworth 2006; Yoshimitsu et al. 2014). However, heterogeneities in shear stress and fault strength along a single fault have been reported (e.g., Allmann and Shearer 2007; Oth 2013). The main rupture areas of large earthquakes exhibit higher static stress drops than surrounding regions, further suggesting variations in fault strength and dynamic stress (Yamada et al. 2010; Urano et al. 2015). The high static stress drops observed around the main rupture area of the 2011 Tohoku-Oki earthquake may indicate the presence of a high-fault strength barrier that suppressed seismic slip in surrounding areas (Uchide et al. 2014; Yamada et al. 2021).

Seismicity during earthquake swarms is also influenced by changes in stress and/or fault strength, which manifest as hypocenter migrations and/or static stress drop variations. These changes are induced by perturbations of the pore fluid pressure along a fault due to fluid diffusion and intrusion (e.g., Shapiro et al. 1997; Goertz-Allmann et al. 2011; Shelly et al. 2013; Yamada et al. 2015; Hainzl et al. 2016; Yoshida et al. 2019; Ross and Cochran 2021), as well as aseismic slip (e.g., Takada and Furuya 2010; Lengliné et al. 2014; Himematsu and Furuya 2015; Ruhl et al. 2016; Yamada et al. 2017; De Barros et al. 2020; Yukutake et al. 2022; Jeong et al. 2024). In addition, some swarms had been triggered by the combination of the fluid diffusion and aseismic slip (e.g., De Barros et al. 2020; Hatch et al. 2020).

Around mid-2018, the number of earthquakes in and around the northeastern Noto Peninsula began to increase, and from around December 2020, seismicity intensified into an earthquake swarm. This swarm comprised four clusters of seismicity that occurred successively in the south, west, north, and east of the study area (hereafter referred to as clusters S, W, N, and E, respectively) (Fig. 1). A M_{JMA} 6.5 earthquake occurred at the northern tip of cluster E on 5 May 2023, and the hypocenter of the M_{JMA} 7.6 earthquake on 1 January 2024 was located between clusters S and N.

Seismic, geodetic, and electromagnetic studies conducted to elucidate the cause of this earthquake swarm suggest that it was likely driven by fluid migration. Amezawa et al. (2023) used precise hypocenter relocations to show that the hypocenter migrations followed a fluid diffusion model (Shapiro et al. 1997). They suggested that fluids rising from the deep part of cluster S spread to clusters W, N, and E, leading to intensified seismic activity. Yoshida et al. (2023) confirmed results of Amezawa et al. (2023) by analyzing seismological data. Nishimura et al. (2023) modeled crustal deformation based on multiple GNSS datasets and precise hypocenter distributions; the overall displacement pattern from December 2020 to December 2022 showed horizontal expansion and uplift centered around

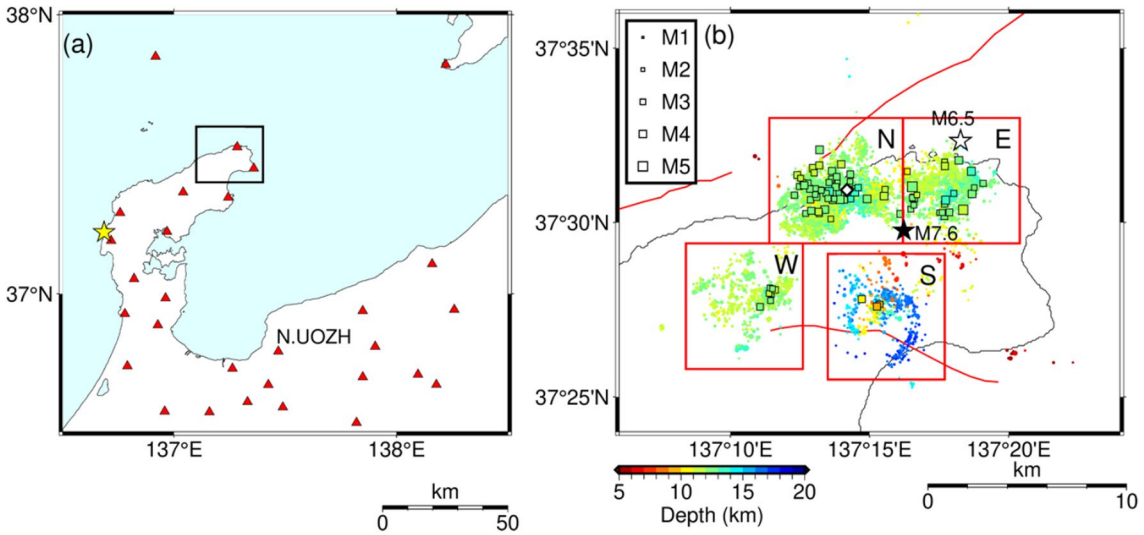

Fig. 1 **a** The distribution of seismic stations (triangles) used in this study. The square indicates the area shown in **b**. The yellow star indicates the epicenter of the 2007 Noto-Hanto earthquake. **b** The distribution of relocated earthquake hypocenters (circles colored according to source depth) from January 2018 to November 2022 ($M_{JMA} \geq 1.2$) (Nishimura et al. 2023). Red squares delineate the four clusters (S, W, N, and E). Squares indicate earthquakes analyzed in this study. The open diamond is the epicenter of the event for which seismograms are shown in Fig. 2. The white and black stars are the location of the 5 May 2023 *M*6.5 and 1 January 2024 *M*7.6 earthquakes reported by JMA, respectively. Red lines show active faults in the area (Inoue and Okamura 2010; Ozaki 2010)

the epicentral region of the earthquake swarm. They proposed that fluids ascending from the deep part of cluster S spread through a southeast-dipping permeable fault zone, causing fault opening and aseismic slip. They also showed that the Coulomb stress change due to the fault opening and aseismic slip, as well as up-dip diffusion of fluids, triggered seismic activity on shallower faults in the area, namely in clusters W, N, and E. A fluid-rich zone in the lower crust beneath cluster S was identified based on the existence of a low-resistivity zone (Yoshimura et al. 2023) and a low-velocity zone there (Nakajima 2022; Matsubara et al. 2022; Okada et al. 2024). Moreover, Okada et al. (2024) suggested the existence of a Tertiary magma reservoir releasing fluids in the lower crust beneath cluster S from high V_P and high V_P/V_S anomalies.

In this study, we investigated the spatiotemporal distribution of static stress drops associated with the northeastern Noto Peninsula earthquake swarm. We focused on the relationship between hypocenter migration on the source fault and the static stress drop over a specified time in the earthquake swarm. As this swarm was likely driven by fluid migration (Amezawa et al. 2023; Yoshida et al. 2023), it provides good opportunity for investigating the effect of pore pressure increase on stress drop estimates of triggered earthquakes. We elucidate the role of fluid on the heterogeneous distribution of static stress drops in this earthquake swarm.

2 Data and method

For our analyses, we selected 90 target earthquakes ($3.0 \leq M_{JMA} \leq 5.4$) that occurred in and around the northeastern Noto Peninsula between 1 January 2018 and 30 November 2022 and consisted of four clusters of the earthquake swarm (Fig. 1b). In this period, as mentioned below, a precise hypocenter dataset was provided by Nishimura et al. (2023). The depth range of selected 90 earthquakes was between 9.9 and 13.34 km (Table 1). We used P- and S-wave arrival times reported by the Japan Meteorological Agency (JMA) and velocity waveform data recorded at permanent seismic stations operated by the JMA, the Hi-net of the National Research Institute for Earth Science and Disaster Resilience (NIED), the Earthquake Research Institute, the University of Tokyo, and the Disaster Prevention Research Institute, Kyoto University (Fig. 1a). The number of stations used in this study is 29. Each seismometer had a natural frequency of 1 Hz and a sampling frequency of 100 Hz. Epicentral distances between target earthquakes (TEQs), of which corner frequency is estimated as described below, and stations ranged from 0.9 km to 113 km.

To estimate the corner frequencies of the target earthquakes by applying the empirical Green's function (EGF) method following Yamada et al. (2021), we selected nearby hypocenters from the hypocenter dataset of Nishimura et al. (2023), which they relocated using the double-difference method (Waldhauser and Ellsworth 2000) and the JMA velocity structure model (Ueno et al.

Table 1 Origin times, hypocentral locations, estimated corner frequencies, seismic moments, and static stress drops for the 90 earthquakes analyzed in this study. Values in parentheses indicate two standard deviations on the logarithmic means of the static stress drops

Origin time (JST)	Latitude (°N)	Longitude (°E)	Depth (km)	M_{JMA}	f_C^P (Hz)	f_C^S (Hz)	M_0 ($\times 10^{14}$ Nm)	$\Delta\sigma_P$ [a] (MPa)	$\Delta\sigma_S$ [a] (MPa)
2019/08/27 23:58	37.4635	137.2453	10.01	3.8	2.9	2.4	3.06[b]	3.89 (0.613–9.24)	9.7 (0.587–22.3)
2021/05/30 14:24	37.4658	137.1911	12.02	3.1	4.4	4.5	0.562	3 (0.823–10.9)	9.8 (0.649–26.6)
2021/06/26 12:24	37.5110	137.2345	12.74	4.1	4.1	3.0	3.64[b]	11.7 (4–27.5)	16.7 (4.2–33.6)
2021/07/11 09:16	37.5041	137.2685	12.27	3.9	4.7	3.1	4.07[b]	23.3 (1.33–52.1)	17.3 (14.3–22.1)
2021/07/11 16:24	37.5113	137.2388	13.01	3.3	6.5	3.8	1.12	15.1 (2.71–29.1)	9.9 (3.18–15.7)
2021/08/04 22:13	37.4598	137.1844	12.44	3.6	3.8	3.6	1.81[b]	4.23 (1.15–9.22)	12.5 (8.55–22.2)
2021/08/11 17:43	37.4689	137.1903	12.16	3.0	6.4	5.6	0.398	5.02 (0.224–8.62)	16.7 (1.26–35.2)
2021/08/13 16:50	37.5156	137.2206	12.62	3.2	4.0	3.9	0.794	2.2 (0.964–3.36)	8.1 (1.39–18)
2021/08/13 19:30	37.4679	137.1934	11.84	3.5	5.0	3.4	2.24	12.1 (6.76–23.9)	14.7 (6.35–48.1)
2021/08/13 20:46	37.4662	137.1898	11.93	3.1	4.5	4.8	0.562	2.14 (0.503–5.2)	10.6 (2.19–20.3)
2021/08/14 22:38	37.5062	137.2231	12.87	4.2	3.9	2.2	25.1	69 (40.2–152)	43.7 (12.2–63.6)
2021/08/18 12:03	37.4628	137.1907	12.41	3.2	4.7	4.4	0.794	5.4 (0.789–12.6)	12.7 (1.06–26)
2021/08/21 16:40	37.5155	137.2364	12.68	3.7	3.0	2.0	2.9[b]	3.5 (0.958–10.2)	3.85 (1.16–5.86)
2021/08/21 16:48	37.5139	137.2348	12.68	3.1	6.5	7.1	0.562	12.6 (1.76–43.7)	34.3 (5.59–63.1)
2021/08/21 16:57	37.5043	137.2117	12.33	3.2	5.3	3.2	0.794	5.7 (1.64–12.1)	5.7 (0.668–30)
2021/09/07 14:07	37.5108	137.2281	12.81	4.2	2.7	2.5	6.41[b]	6.4 (0.881–18)	17.1 (7.39–30.3)
2021/09/16 18:42	37.5060	137.3061	11.98	5.1	1.8	1.0	301[b]	87 (21.2–216)	57 (3.95–253)
2021/09/16 19:01	37.5089	137.2949	12.17	3.5	4.8	3.9	2.24	10.8 (2.22–17.8)	32 (0.709–142)
2021/09/17 04:40	37.5047	137.2919	12.01	3.0	5.4	4.9	0.398	3.39 (0.583–8)	8.6 (2.46–20.5)
2021/10/03 11:10	37.5110	137.2323	12.62	4.3	2.6	1.8	4.52[b]	3.64 (1.07–7.9)	3.8 (0.867–6.03)
2021/10/03 12:38	37.5153	137.2366	12.80	3.2	4.0	4.0	0.794	2.35 (0.569–5.99)	9.7 (2.25–27.3)
2021/10/03 14:43	37.5158	137.2370	12.83	3.8	4.9	1.3	4.52[b]	24.8 (7.24–48.3)	1.94 (0.652–4.47)
2021/10/03 21:31	37.5160	137.2416	12.93	3.3	5.0	4.4	1.12	6.3 (0.804–13.1)	14.9 (5.3–25.5)
2021/10/05 21:09	37.5143	137.2391	12.94	3.5	4.7	3.7	2.24	11.5 (2.99–26.2)	19 (7.09–40.3)
2021/10/26 23:48	37.5196	137.2384	12.64	3.0	5.0	2.9	0.398	3.1 (0.483–13.5)	1.82 (0.426–5.59)
2021/11/02 06:17	37.5180	137.2300	12.38	3.6	6.4	1.7	2.29[b]	38 (0.382–82.6)	1.92 (0.906–3.06)
2021/11/02 08:08	37.5194	137.2305	12.36	3.3	8.6	6.7	1.12	30.5 (20.1–48.5)	50 (19–71)
2021/11/02 19:06	37.5169	137.2295	12.47	3.9	2.3	2.6	2.33[b]	1.44 (0.32–2.83)	6.1 (2.3–11)
2021/11/04 22:44	37.5147	137.2247	12.21	3.5	4.4	3.0	1.22[b]	4.83 (1.34–8.73)	4.94 (1.63–7.54)
2021/11/05 00:21	37.5136	137.2277	12.49	4.0	3.8	1.7	4.93[b]	12.1 (4.9–20.9)	5.3 (0.518–14)
2021/11/15 10:04	37.5231	137.2385	12.27	3.6	5.4	4.0	1.08[b]	7.9 (1.31–17.1)	11.2 (5.6–19.5)
2021/12/03 03:41	37.5202	137.2275	12.11	3.3	4.1	3.6	1.12	3.72 (1.5–7.61)	8.1 (1.97–17.9)
2021/12/07 20:41	37.5209	137.2273	12.06	3.2	—	4.6	0.794	—	11.8 (7.33–19.1)
2021/12/07 20:43	37.5192	137.2258	12.03	3.4	7.5	6.3	1.58	35.9 (10.2–76.9)	56 (25.3–143)
2021/12/31 14:52	37.5146	137.2411	13.34	4.3	4.0	2.7	6.89[b]	20.4 (8.36–39.5)	20.8 (5.79–42.6)
2022/01/04 19:41	37.5108	137.2147	12.37	3.5	4.3	4.0	2.24	10.1 (5.84–25.1)	23.8 (4.46–40.3)
2022/01/14 13:11	37.5122	137.2183	12.66	3.6	4.4	3.1	3.16	17.1 (2.54–44.2)	13.9 (6.3–36.2)
2022/02/07 17:59	37.5113	137.2485	12.94	4.1	3.5	3.0	4.58[b]	8.4 (3.67–13.8)	20.1 (6.11–36.2)
2022/02/22 19:55	37.4684	137.1919	12.12	3.0	—	6.9	0.398	—	18.8 (17.3–21.4)
2022/02/23 14:17	37.5017	137.2268	11.32	3.0	3.6	1.9	0.398	1.59 (0.054–7.5)	1.1 (0.041–11.2)
2022/03/07 16:36	37.4610	137.2561	9.90	3.4	—	2.2	1.58	—	3.75 (0.936–9.8)
2022/03/08 01:06	37.4599	137.2544	9.96	3.9	—	2.0	8.91[b]	—	15.1 (0.937–46.2)
2022/03/10 17:24	37.5029	137.2948	12.44	3.6	4.0	4.3	1.24[b]	3.38 (1.36–6.32)	16.1 (4.83–34.9)
2022/03/10 19:32	37.5049	137.2978	12.48	3.7	4.2	2.3	1.91[b]	7.2 (1.22–19.5)	3.61 (2.2–4.84)
2022/03/11 03:13	37.5048	137.2935	12.35	3.3	8.6	7.6	1.12	39 (3.39–87.2)	74 (48.7–107)
2022/03/12 19:00	37.5139	137.3004	13.06	3.3	—	6.2	1.12	—	57 (0.795–134)
2022/03/20 03:32	37.5164	137.2142	12.24	3.1	6.3	4.3	0.562	7.2 (2.09–22.9)	8.7 (0.863–24.4)

Table 1 (continued)

Origin time (JST)	Latitude (°N)	Longitude (°E)	Depth (km)	M_{JMA}	f_C^P (Hz)	f_C^S (Hz)	M_0 ($\times 10^{14}$ Nm)	$\Delta\sigma_P$ [a] (MPa)	$\Delta\sigma_S$ [a] (MPa)
2022/03/23 09:23	37.5107	137.2955	13.07	4.3	3.2	1.5	18.1[b]	34 (2.49–104)	11.3 (2.61–27.8)
2022/03/27 16:15	37.5134	137.2175	12.58	3.0	10.0	8.5	0.398	18.5 (3.5–43.6)	42 (8.07–109)
2022/04/04 10:26	37.5149	137.2259	13.30	4.3	2.8	2.0	13.5[b]	19 (5.09–68.8)	18.4 (7.97–34.2)
2022/04/04 10:28	37.5186	137.2127	12.20	4.0	3.9	3.5	4.07[b]	10.7 (5.96–23.3)	26.5 (17.5–37.6)
2022/04/04 10:30	37.5139	137.2240	12.69	3.4	—	3.7	1.58	—	12.8 (6.17–26.9)
2022/04/04 11:18	37.5227	137.2067	11.67	3.7	3.1	4.1	2.33[b]	3.12 (1.16–6.54)	21.7 (13.2–34.9)
2022/04/08 22:04	37.5117	137.2765	12.32	4.2	2.5	1.6	18.3[b]	14.5 (3.66–37.8)	12.1 (4.56–28.1)
2022/04/08 22:29	37.5118	137.2757	12.14	3.3	5.1	4.0	1.12	6.13 (4.17–9.87)	10.6 (6.36–15.7)
2022/04/08 22:36	37.5132	137.2784	11.98	3.0	4.1	4.5	0.398	1.18 (0.483–1.91)	5.43 (3.15–6.35)
2022/05/25 21:51	37.5131	137.2050	12.11	3.4	—	4.9	1.58	—	47 (6.17–184)
2022/06/03 00:22	37.5172	137.2080	12.16	3.3	5.7	3.8	1.12	11.8 (1.36–27.1)	11.9 (1.2–36.7)
2022/06/03 13:29	37.5246	137.2275	12.10	3.9	3.0	3.0	4.07[b]	4.95 (1.77–8.4)	18.9 (7.14–46.7)
2022/06/10 03:05	37.5218	137.2303	12.18	3.5	5.8	4.5	2.24	21.1 (2.46–50.3)	47 (2.58–147)
2022/06/12 18:14	37.5113	137.2288	12.96	3.0	3.6	2.6	0.398	0.87 (0.483–1.58)	1.06 (0.532–3.15)
2022/06/12 20:00	37.5115	137.2251	12.85	3.4	3.7	3.3	1.58	3.72 (1.14–8.07)	10.1 (2.43–26.9)
2022/06/16 02:27	37.5278	137.2330	11.99	4.0	1.9	1.9	4.27[b]	1.76 (0.301–8.12)	5.5 (1.69–12.1)
2022/06/19 15:08	37.5171	137.2756	12.68	5.4	1.3	0.9	612[b]	69 (8.55–123)	94 (19.1–242)
2022/06/19 15:19	37.5064	137.2747	12.76	3.2	5.3	6.1	0.794	6.8 (1.22–12.1)	37 (1.39–105)
2022/06/19 16:38	37.5158	137.2593	11.21	3.3	4.6	4.1	1.12	4.96 (1.5–9.39)	11.4 (5.81–15.7)
2022/06/19 19:22	37.5244	137.2726	10.90	3.2	3.7	3.4	0.794	2.01 (0.569–4.55)	7.3 (0.785–36)
2022/06/20 10:41	37.5167	137.3127	12.74	3.0	4.6	5.2	0.398	1.8 (0.757–3.33)	13.6 (0.099–55.7)
2022/06/20 14:50	37.5245	137.3110	13.52	4.3	4.3	2.6	5.35[b]	20.7 (4.79–59.9)	14.5 (6.17–23)
2022/06/21 03:13	37.5083	137.2765	12.58	3.0	5.8	3.9	0.398	5.4 (0.789–18.8)	4 (0.611–10.4)
2022/06/21 10:42	37.5126	137.2587	11.54	4.1	3.1	2.6	8.50[b]	10.7 (4.79–20.5)	22.7 (6.02–40.2)
2022/07/17 20:51	37.5167	137.2432	13.00	3.4	6.4	5.6	1.58	19.3 (9.08–31.8)	49.6 (1.33–92.6)
2022/08/14 19:14	37.5259	137.2162	11.86	4.1	3.2	2.0	4.84	7.6 (3.08–20.5)	6.2 (2.86–12.3)
2022/08/14 19:28	37.5273	137.2198	11.86	3.9	4.1	2.8	8.91	34.8 (5.02–90.8)	44 (2.82–133)
2022/08/16 17:55	37.5238	137.2168	11.99	3.4	5.1	6.5	1.58	11.2 (2.77–25.1)	79 (6.17–172)
2022/08/29 22:25	37.5193	137.2100	12.00	3.1	4.0	3.6	0.562	2.09 (0.279–4.47)	4.7 (0.473–12.8)
2022/09/14 08:54	37.5160	137.2142	12.29	3.5	4.6	4.5	1.13[b]	5.16 (2.73–9.95)	14.9 (7.6–22.9)
2022/09/20 15:05	37.5290	137.2950	11.69	3.1	7.2	4.5	0.562	9.8 (3.81–20.9)	8.9 (1.6–19.3)
2022/09/25 06:23	37.5270	137.2951	11.89	3.8	2.9	1.7	4.14[b]	5.1 (0.569–11.6)	3.21 (2.01–4.09)
2022/09/28 06:21	37.5052	137.2195	11.10	3.8	3.5	3.3	2.48[b]	4.8 (1.58–8.61)	14.3 (3.31–39.5)
2022/10/25 07:08	37.5212	137.2087	11.93	3.2	5.3	3.4	0.794	5.5 (1.92–11.6)	6.6 (0.198–21.2)
2022/11/24 05:13	37.5178	137.2109	12.72	3.9	4.7	3.0	4.19[b]	18.1 (13.6–26.9)	19.1 (5.59–38.7)
2022/11/26 21:58	37.5347	137.2200	12.34	4.2	—	1.7	13.4[b]	—	12 (0.989–26.7)
2022/11/27 15:36	37.5154	137.2211	12.61	3.2	5.8	5.3	0.794	11.4 (0.789–36.4)	22.4 (1.06–54.3)

[a] $\Delta\sigma_P$ and $\Delta\sigma_S$, respectively, indicate static stress drops determined by P-wave and S-wave analyses

[b] Value of the F-net CMT solution

2002). They used the arrival-time differences for event pairs calculated from (i) JMA P- and S-wave arrivals as the catalog data and (ii) cross-spectra of velocity waveforms with average squared coherency equal to or larger than 0.8 in the 1–8 Hz frequency band as the correlation data (Hayashi and Hiramatsu 2013). This dataset included 7,560 hypocenters with $M_{JMA} \geq 1.2$ that occurred during January 2018 to November 2022.

For each target earthquake, we selected EGF earthquakes with hypocenters within a 1 km radius and lower in magnitude by at least 0.5. It is appropriate for an EGF to be located within approximately one source dimension of a TEQ (Abercrombie 2015). The selection of EGFs within a 1 km radius from a TEQ may be too large compared to the source radius of a magnitude 3 event of about 150 m. However, 90% and 67% of EGFs for P-waves, and 87% and

64% for S-waves, were distributed within radii of 0.5 km and 0.3 km, respectively (Additional file 1: Fig. S1). Therefore, the majority of EGF events used in this study adhered to the criterion of TEQ–EGF distance proposed by Abercrombie (2015). The magnitudes (M_{JMA}) of the selected EGF earthquakes ranged from 2.2 to 4.2.

For P-waves, we analyzed the vertical component of each velocity waveform using three moving time windows (Imanishi and Ellsworth 2006), each of 2.56 s length and with time shifts of 0.16 s. For S-waves, we analyzed the horizontal components of each velocity waveform using three moving time windows, each of 5.12 s length and with time shifts of 0.64 s (Fig. 2). For earthquakes of magnitude ≥ 5, the S-wave time window length was extended to 10.23 s. To obtain the noise spectrum, we set the end of the time window to 0.5 s prior to the arrival of the P-wave and its length to be the same as the associated P- or S-wave time window. Shorter time windows, such as 1.28 s for P-waves and 1.28 s and 2.56 s for S-waves, revealed an apparent magnitude dependence on the estimated static stress drops. This suggests inadequate estimates of the corner frequencies of TEQs for larger events (Additional file 1: Fig. S2).

Of the 90 target earthquakes, 8 earthquakes could not be used for P-wave analysis because of their short S–P times and low signal-to-noise ratios (S/N). Of the remaining 82 target earthquakes suitable for P-wave analysis, multiple EGF earthquakes were available, and thus used, for 46 events. All 90 target earthquakes were suitable for S-wave analysis; of those, multiple EGF earthquakes were available, and thus used, for 27 events. Most target earthquakes were analyzed with only a single EGF earthquake, although 2 to 5 EGF earthquakes were available for 46 target events in P-wave analysis and 27 target events in S-wave analysis (Additional file 1: Fig. S3). The average number of EGF earthquakes used for a single target event was 1.8 in P-wave analysis and 1.5 in S-wave analysis.

The deconvolved velocity amplitude spectrum, $\dot{u}_r(f)$, is approximated as (Boatwright 1978):

$$|u_r(f)| \approx R_r M_{or} \left(\frac{1+(f/f_{CE})^4}{1+(f/f_{CT})^4}\right)^{1/2}, \quad (1)$$

where $R_r = R_T/R_E$ and $M_{0r} = M_{0T}/M_{0E}$ are the ratios of the radiation pattern coefficients and the seismic moments of target and EGF earthquakes, respectively, and f_{CT} and f_{CE} are the corner frequencies of target and EGF earthquakes, respectively.

Taking the logarithm of Eq. (1) provides the linear relationship:

$$\begin{aligned}\ln\left(\left|\dot{u}_r(f)\right|\right) =& \ln(R_r M_{0r}) - \frac{1}{2}\ln\left(1+\left(f/f_{CT}\right)^4\right) \\ &+ \frac{1}{2}\ln\left(1+\left(f/f_{CE}\right)^4\right).\end{aligned} \quad (2)$$

We searched for the optimum values of f_{CT}, f_{CE}, and $R_r M_{0r}$ that minimize the sum of squared residuals between the observed spectral ratios from the three moving windows and a spectral ratio calculated using a grid search (Fig. 2). In the grid search, the search ranges and grid intervals for f_{CT}, f_{CE}, and $\ln(R_r M_{0,r})$ were 0.1–20 Hz and 0.1 Hz, 0.2–26 Hz and 0.1 Hz, and 0.3–4 and 0.05, respectively. However, reliable estimates for f_{CE} was difficult because of the 100 Hz sampling frequency of the seismometers used, particularly for smaller earthquakes. Consequently, in this study, we estimated the static stress drop for the target earthquakes from f_{CT}.

We visually inspected the fitting of the observed and theoretical spectral ratios and excluded poorly fitting cases: only target events with corner frequency estimates at five or more stations, including cases with multiple EGF earthquakes, were used for the following further analyses.

The seismic moment (M_0) values for 37 target events with available CMT solutions from the NIED-operated F-net were adopted directly. For other earthquakes, we used the equation $\log_{10} M_0 = 1.5 M_w + 9.1$ (Hanks and Kanamori 1979) to estimate M_0, assuming $M_w = M_{JMA}$ (Urano et al. 2015). The static stress drops estimated from P-waves ($\Delta\sigma_P$) and S-waves ($\Delta\sigma_S$) were determined as (Madariaga 1976):

$$\Delta\sigma_p = \frac{7}{16} M_0 \left(\frac{f_{CT}}{0.32 Vs}\right)^3, \text{ and } \Delta\sigma_s = \frac{7}{16} M_0 \left(\frac{f_{CT}}{0.2 W_s}\right)^3, \quad (3)$$

where we adopted an S-wave velocity V_S of 3.2 km/s, as previously used to estimate the static stress drops of the aftershocks of the 2007 Noto-Hanto earthquake in the northwestern Noto Peninsula (Urano et al. 2015).

For each analyzed earthquake, we calculated the logarithmic mean of the estimated static stress drops from P-waves and S-waves over all stations as the static stress drops from P-waves and S-waves for that event.

3 Results and discussion

3.1 Overall characteristics of static stress drops of the earthquake swarm in the northeastern Noto Peninsula

The corner frequencies we obtained are consistent with the scaling relationship between corner frequency and seismic moment ($M_0 \propto f_{CT}^{-3}$) (Additional file 1: Fig. S4) reported in previous studies (e.g., Hiramatsu et al. 2002; Imanishi and Ellsworth 2006; Yoshimitsu et al. 2014). All estimated values are summarized in Table 1. The

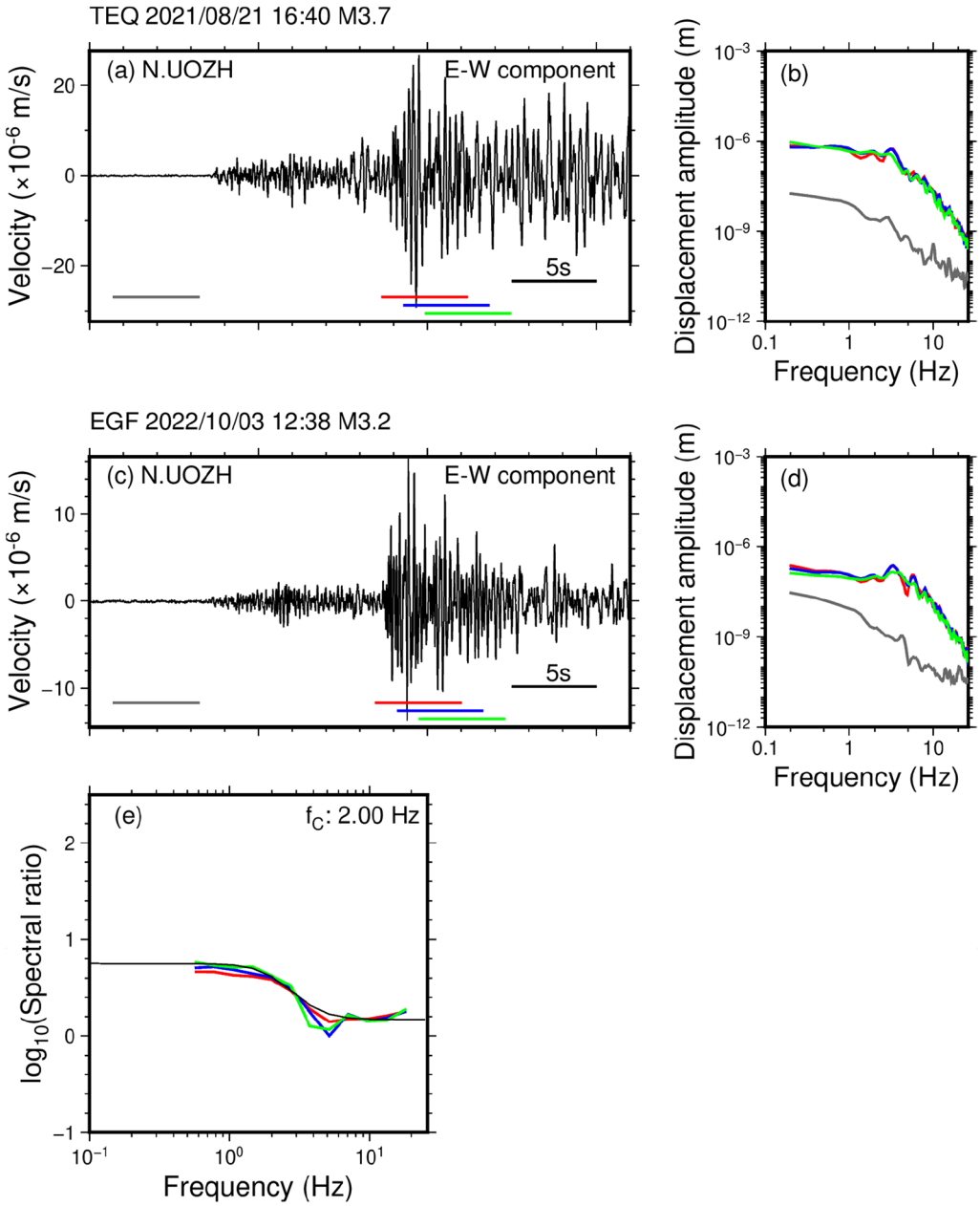

Fig. 2 **a** S-wave seismogram of a *M*3.7 target earthquake (TEQ, open diamond in Fig. 1b) recorded at station N.UOZH (Fig. 1a). Colored lines indicate the three 5.12-s time windows used for deconvolution, which were (red) − 0.50 to + 4.62 s, (blue) 0.14 to 5.26 s, and (green) 0.78 to 5.90 s after S-wave arrival. The gray line indicates the time window from 5.62 to 0.5 s before P-wave arrival, used to determine the noise level. **b** Displacement amplitude spectra of the waveforms for the four time windows marked in **a**. **c** S-wave seismogram of a *M*3.2 EGF earthquake (EGF) recorded at station N.UOZH (time windows marked as in **a**). **d** Displacement amplitude spectrum of the waveforms for the four time windows marked in **c**. **e** Deconvolved spectra for the individual three time windows (colored lines) with the fitted model of Eq. (2) (black line)

static stress drops estimated from P-waves ranged from 0.60 to 94 MPa (logarithmic mean of 13 MPa) and those from S-waves ranged from 1.1 to 94 MPa (logarithmic mean of 19 MPa), which are typical values for crustal earthquakes. There are, however, slight differences in the static stress drops estimated from P-waves and S-waves. This is mainly because the assumed rupture speed in this study (0.9 Vs) (Madariaga 1976) might be faster than the real one (Yamada et al. 2017). The S/N

for P-waves was generally lower than that for S-waves. Additionally, the time window for P-waves was shorter than that for S-waves. Therefore, we consider the static stress drops estimated from S-waves to be more reliable than those estimated from P-waves.

In this study, EGFs were selected within a 1 km radius from a TEQ. EGFs located outside one source dimension of a TEQ might introduce a systematic difference in static stress drops. To investigate this, we compared f_{CT} estimated from each EGF for a given TEQ (Additional file 1: Fig. S1). The difference, Δf_{CT}, between the average f_{CT} over all EGFs and f_{CT} estimated from each EGF for a given TEQ, indicates no systematic variation in f_{CT} with the distance between an EGF and a TEQ. However, the distribution of Δf_{CT} for P-waves shows greater scatter compared to that for S-waves, suggesting potentially less reliable estimates from P-waves than from S-waves.

We used the Boatwright spectral model due to its characteristic of sharp spectral ratio decay proportional to f^{-2}. This property lowers the uncertainty in estimating the corner frequency, thereby reducing errors in the stress drop analysis compared to the Brune spectral model (Brune 1970). However, the selection of a spectral model modifies results of EGF analysis. Previous studies have highlighted differences in corner frequencies that hinge on the choice of spectral models (Huang et al. 2016; Yamada et al. 2021). As demonstrated in Huang et al. (2016), estimates of f_{CT} derived from the Boatwright spectral model are smaller than those from the Brune spectral model (Additional file 1: Fig. S5), resulting in lower static stress drops calculated using the Boatwright spectral model than the Brune spectral model. Moreover, the disparity in f_{CT} is more pronounced for P-waves than for S-waves, suggesting potentially greater variability in estimates from P-waves than from S-waves.

3.2 Spatial heterogeneity of static stress drops among clusters

The spatial distribution of static stress drops in each cluster were heterogeneous, especially in clusters N and E (Fig. 3). The logarithmic mean static stress drops we estimated from P-waves and S-waves for each cluster were, respectively, 7 MPa and 12 MPa in cluster N, 9 MPa and 14 MPa in cluster E, 5 MPa and 13 MPa in cluster W, and 4 MPa and 8 MPa in cluster S (Table 2). In clusters N and E, earthquakes had larger static stress drops. However, considering the limited number of estimated static stress drops in clusters S and W, this might simply result from a wide scatter among observed static stress drops. Consequently, we cannot confirm distinct differences in static stress drops among the individual clusters.

3.3 Relationship between the distribution of static stress drops and source faults

The static stress drop on a fault is crucial for monitoring fault strength, which can be affected in space and time by fluid diffusion (e.g., Yamada et al. 2015; Yoshida et al. 2019). Generally, an earthquake occurs when stress gradually increases over a long period and reaches the shear strength of a fault. However, when fluid is involved, the shear strength decreases rapidly as the pore pressure increases. When shear strength equals the stress, an earthquake occurs. Behind the fluid diffusion front, the pore pressure has increased sufficiently, allowing earthquakes to occur at lower shear strengths. Therefore, the static stress drop, approximately given by the difference between shear strength and dynamic frictional stress, is small (Yamada et al. 2015).

A clear migration of hypocenters, possibly driven by fluid diffusion, has been observed for the earthquake swarm in the northeastern Noto Peninsula (Amezawa et al. 2023; Yoshida et al. 2023). Therefore, variations in fault strength, likely influenced by pore fluid pressure, can be assessed by examining changes in the static stress drop along a fault over a given period.

If the source fault of the earthquake swarm comprises a single fault plane, it is straightforward to discern such variations in static stress drop by analyzing the depth distribution and/or planar spatiotemporal distribution. However, for earthquakes occurring on multiple faults, such a straightforward investigation may not provide reliable constraints. Thus, we scrutinized the spatiotemporal distribution along cross sections of the prominent dip direction within cluster N, focusing on source faults clearly delineated by the relocated hypocenter distribution. Clusters S, W, and E are omitted from further discussion owing to the limited number of earthquakes for which we could estimate static stress drops and the relatively low resolution of hypocenter alignments in cross sections in those clusters.

The depth and magnitude dependence of static stress drops may cause apparent spatiotemporal variations in static stress drops if analyzed events accompanied by systematic variations in depth and magnitude. In cluster N, most events are distributed at depths of approximately 12 to 13 km and no depth-dependent variation in static stress drops is observed (Additional file 1: Fig. S6). Similarly, no magnitude-dependent variation in static stress drops is observed (Additional file 1: Fig. S7). Hence, we infer that there is no variation in static stress drops due to these two factors for events in cluster N.

Figure 4 illustrates the progression of the spatial distribution of static stress drops estimated from S-waves for earthquakes along a single fault in profile L2 in the

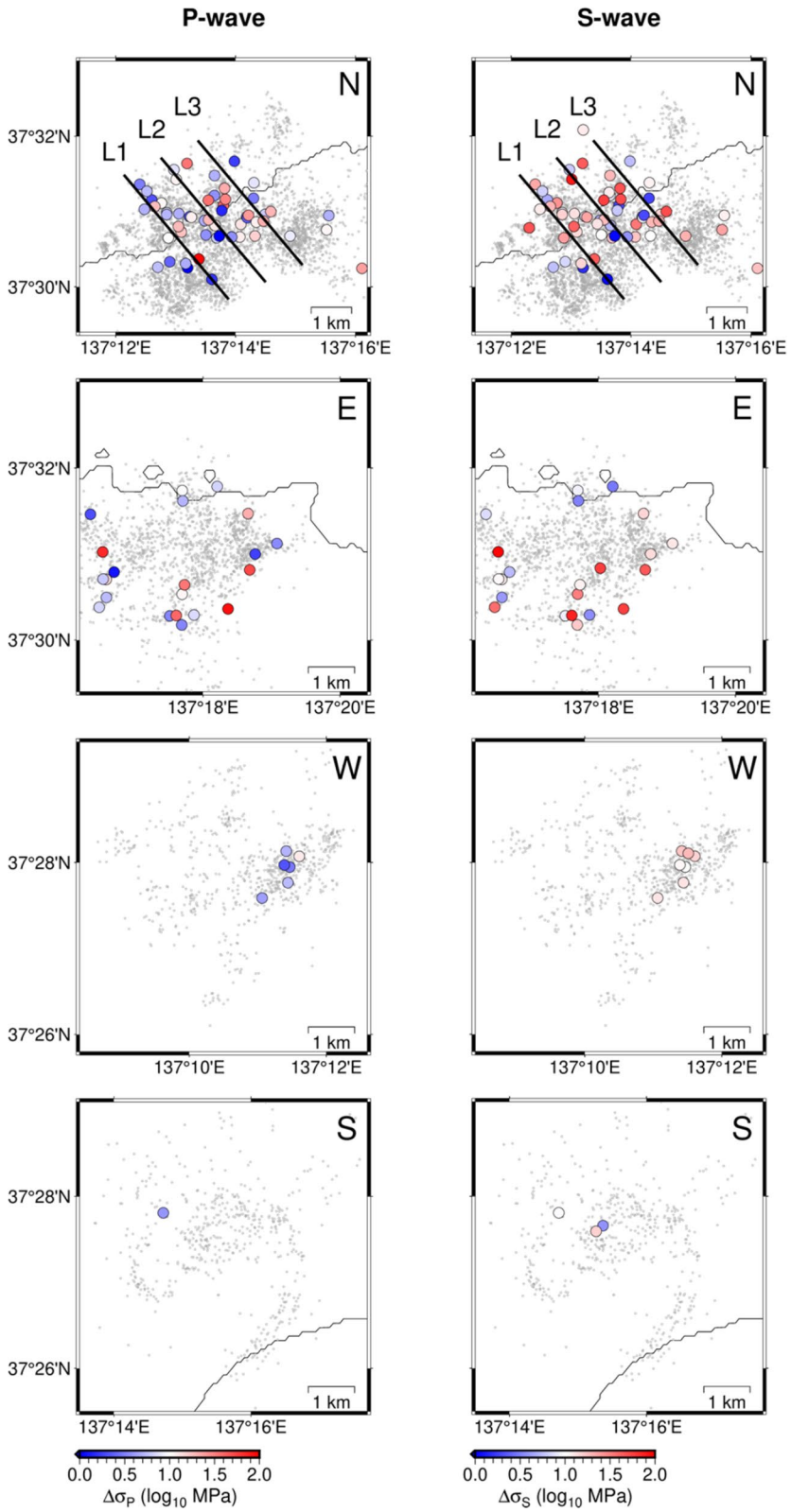

Fig. 3 Spatial distribution of static stress drops estimated from P-waves (left panels) and S-waves (right panels) for each cluster. Black lines are profiles L1, L2, and L3, along which static stress drops are displayed in Figs. 4, S5, and S6

Table 2 The logarithmic means of static stress drops for each cluster (N, E, W, S)

	$\Delta\sigma_P$ [MPa][a]	$\Delta\sigma_S$ [MPa][a]	Number P-wave	Number S-wave
N	7.4 (0.5–93)	11 (1.0–78)	54	58
E	9.0 (1.1–87)	14 (2.9–93)	21	22
W	4.5 (2.1–12)	13 (9.8–18)	6	7
S	3.8	8.1 (3.7–15)	1	3

[a] $\Delta\sigma_P$ and $\Delta\sigma_S$, respectively, indicate static stress drops determined by P-wave and S-wave analyses. Values in parentheses indicate the range of estimated static stress drops in each cluster

period from April 2021, that is the beginning of the seismicity in cluster N, to the date cited in each panel. Here we categorized earthquakes for which we calculated static stress drops as those occurring at shallow, medial, and deep parts along the source fault (< 25%, 25–75%, and > 75%), respectively, of the fault length from its shallowest terminus at that time. Because the length of the source fault delineated in our data increased over time, we visually and progressively defined the length of the source fault, indicated by the colored bar, in each panel of Fig. 4. This implies that the shallow, medial, and deep parts along each source fault vary with time on the same fault, ruling out depth dependence of rupture speed as a cause of the difference in static stress drops between the shallow and medial parts.

We investigated the spatiotemporal distribution of static stress drops on two source faults along profile L2 (Fig. 4). Notably, earthquakes with larger static stress drops (e.g., events on 21 August 2021, 7 December 2021, and 14 and 16 August 2022) tended to occur at the shallow, northwest end of the fault plane (red triangles in Fig. 4). In contrast, smaller static stress drops occurred along the medial part of each source fault (e.g., the events on 3 October 2021, 5 November 2021, and 4 April 2022; light red to light blue squares in Fig. 4). Similar trends are observed on source faults in cross sections along profiles L1 and L3 (Additional file 1; Fig. S8), albeit less clearly. To emphasize the disparity between static stress drops in shallow and medial parts of the source faults, we compared the static stress drops of all earthquakes on source faults intersecting the L1, L2, and L3 profiles with those of only shallow (Fig. 5a) and medial earthquakes (Fig. 5b) defined by each time range. We excluded 10 earthquakes without associated source faults from this comparison. Shallower earthquakes had static stress drops skewed towards the higher side of the overall distribution, whereas those of medial earthquakes were skewed towards the lower side of the overall distribution. We also examined temporal variations in static stress drops for events on source faults in the L1, L2, and L3 profiles (Additional file 1: Fig. S9). We found no systematic temporal variation in static stress drops, indicating that the occurrence of events over the entire source faults shows no time dependence. This also implies that our spatiotemporal approach is effective in identifying differences in static stress drops between the temporally varying shallow and medial parts.

Considering the fluctuations among the estimated static stress drops, it is plausible that the observed difference may be a consequence only of the wide scatter among static stress drops. To evaluate the statistical significance of the disparity between the mean static stress drops of earthquakes at shallow and medial depths along the source faults, we conducted a test with the null hypothesis that these means are equal. We applied a non-parametric bootstrap method at a significance level of 5% to the estimated static stress drops of earthquakes on source faults in profiles L1, L2, and L3 combined. Two bootstrap sample sizes were used, set equivalent to the number of earthquakes with observed stress drops on shallow and medial portions of the source faults. The difference between the mean values of the two sampled populations of static stress drops was then calculated. This process was repeated 2,000 times. We estimated the bootstrap p-value for the observed difference in the mean static stress drop values between the shallow and medial fault portions to be 0.0205 (Fig. 5c), which is below 0.05 and leads us to reject the null hypothesis. Therefore, we concluded that the difference in mean static stress drop estimated from S-waves between shallow and medial fault depths is statistically significant.

We also observed larger static stress drops along shallow fault portions and smaller static stress drops along medial portions when we estimated them from P-waves (Additional file 1: Fig. S10), although the differences were smaller than when estimated from S-waves (Additional file 1: Fig. S11). However, the bootstrap p-value was 0.133, indicating that the difference between the mean static stress drops along different fault depths determined from P-waves was not statistically significant (Additional file 1: Fig. S11c). As mentioned in Sect. 3.1, the estimated static stress drops from S-waves were indeed more reliable than those estimated from P-waves. Therefore, we rely solely on the results of our S-wave analysis.

We further examine the choices of EGF on the observed differences between the shallow and medial parts. A 1 km radius for EGF selection is larger than the source dimension of a magnitude 3 event. Selecting EGFs within a 0.5 km radius and a 0.3 km radius provided larger static stress drops in the shallow part than in the medial part

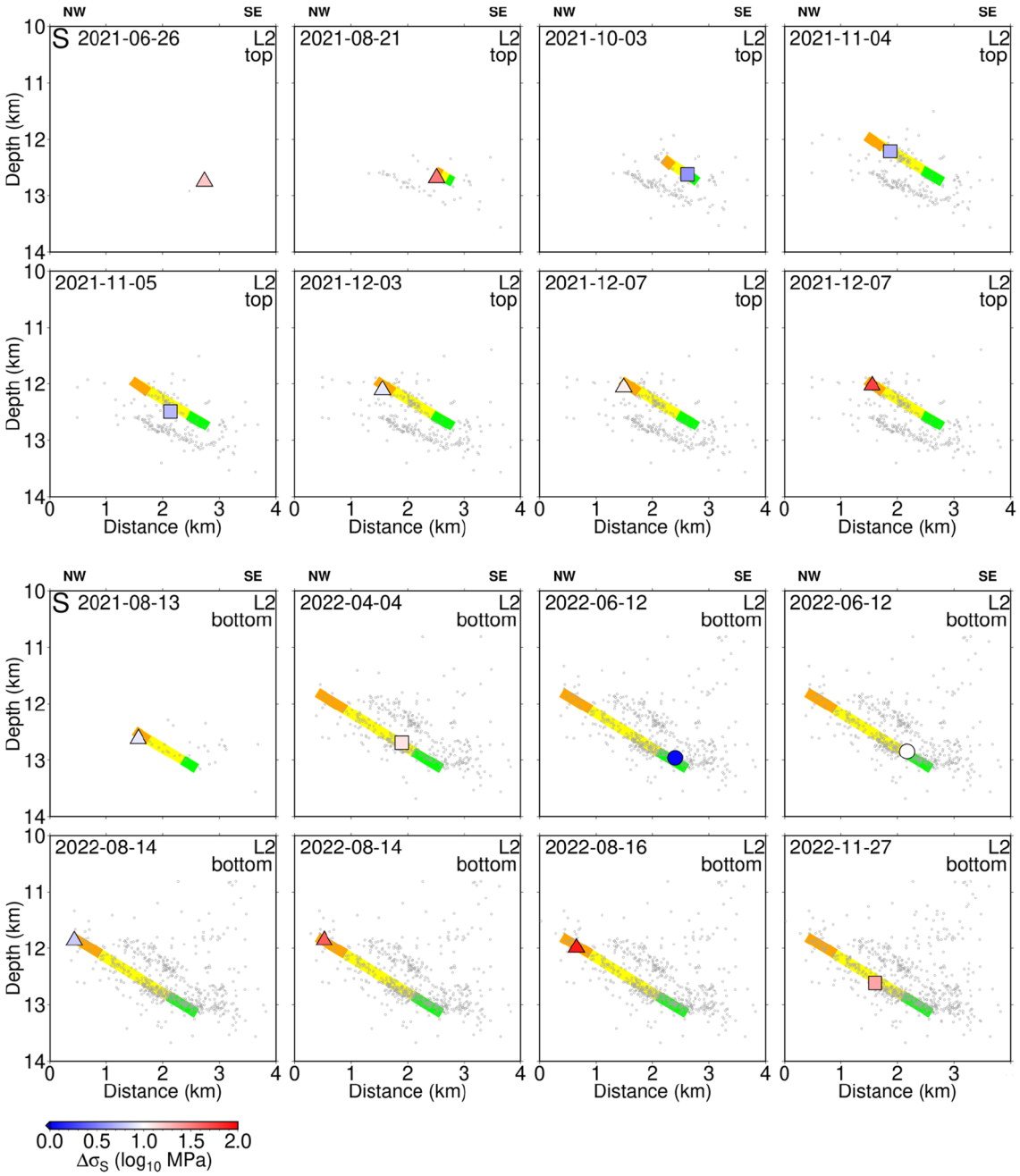

Fig. 4 Spatial distribution of static stress drops from S-wave analysis projected onto vertical cross sections along the L2 profile (within 0.5 km on each side from the line shown in Fig. 3) of cluster N (Figs. 1b, 3). Small gray circles indicate relocated earthquakes that occurred prior to the analyzed earthquake. Bold orange, yellow, and green lines indicate the shallow (within 25% of the overall fault length from the shallowest fault extent up to that date), and medial parts (25–75% of the fault length from the shallowest extent), and the other part, respectively, on source faults of the analyzed earthquakes in each cross section as delineated based on seismicity up to that date. Triangles indicate shallow earthquakes, squares indicate earthquakes at medial parts, and circles indicate deeper earthquakes as determined for the time period from 2018 to the date cited in each panel

with statistical significance in the S-waves analysis as well (Additional file 1: Fig. S12).

A small magnitude difference between EGFs and a TEQ may introduce a bias in the estimates of a corner frequency because a small magnitude difference results in close f_{CT} and f_{CE}, potentially increasing uncertainty in estimating f_{CT}. However, static stress drops obtained from EGFs with a magnitude difference of 1.0 and greater

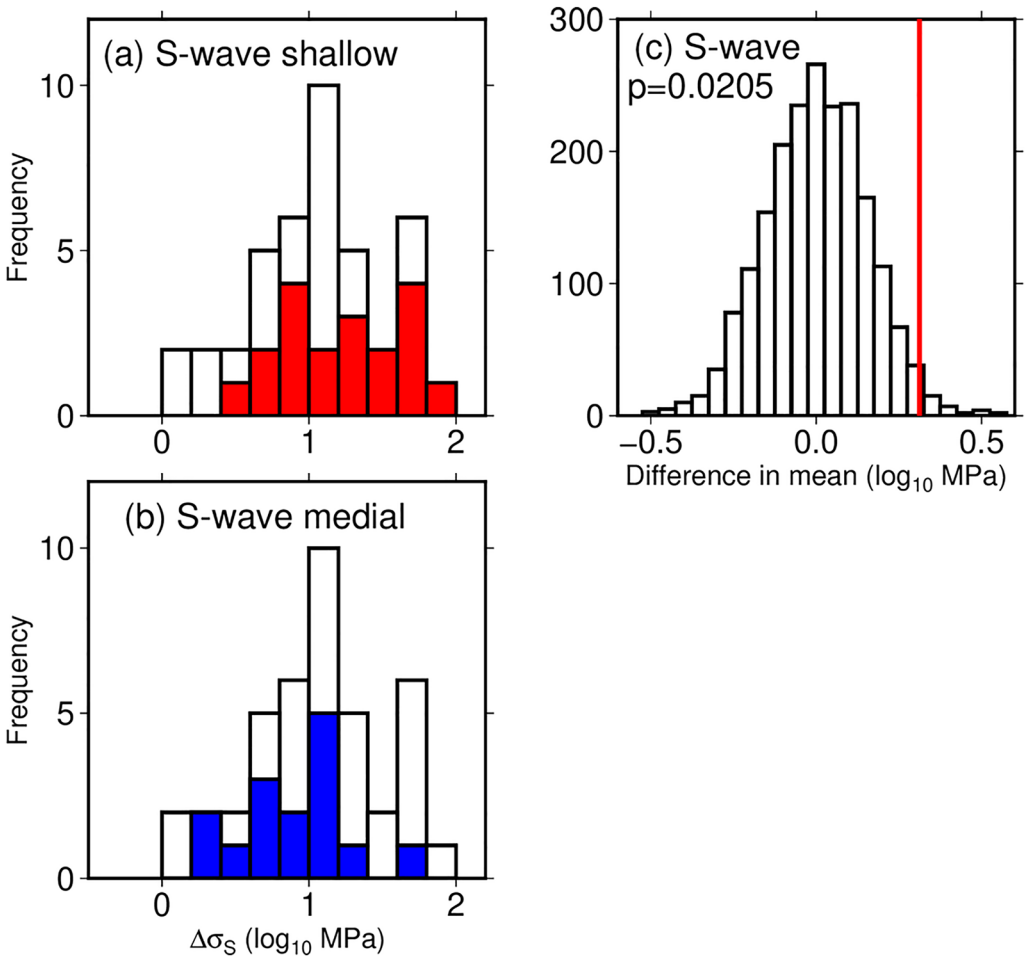

Fig. 5 Comparison of the frequency distributions of static stress drops estimated from S-waves **a** between the earthquakes at shallow parts (red bars) and all earthquakes on the source faults (white bars; see yellow lines in Fig. 4), and **b** between earthquakes at medial parts (blue bars) and all earthquakes on the source faults (white bars). **c** The distribution of the difference between the logarithmic means of the static stress drops of shallow and medial earthquakes obtained by a bootstrap test based on S-wave estimates. The red line indicates the observed difference in the logarithmic mean of the static stress drops

showed similar trends, with larger static stress drops in the shallow parts for both P- and S-waves, and statistically significant results for S-waves (Additional file 1: Fig. S13). Therefore, the criteria for the magnitude difference in the selection of EGFs do not affect the following discussion.

We also examined the frequency distributions of static stress drops of P- and S-waves estimated from f_{CT} of the Brune spectral model (Additional file 1: Fig. S14). We found no difference in static stress drops between the shallow and medial parts for P-waves. For S-waves, we observed larger static stress drops in the shallow part compared to the medial part. A bootstrap test showed a p-value close to the significance level of 0.05. Therefore, we consider that larger static stress drops in the shallow part compared to the medial part could not be rejected, even when using the Brune spectral model.

3.4 The control of fluids on the heterogeneous distribution of static stress drops along source faults

In the northeastern Noto Peninsula earthquake swarm, fluids ascending from the deeper crust (cluster S) primarily diffused towards the southeast-dipping faults in clusters W, N, and E, thereby intensifying seismic activity (Amezawa et al. 2023; Yoshida et al. 2023; Nishimura et al. 2023). The propagation of aseismic slip due to an increase in pore fluid pressure may also contribute to hypocenter migration (Eyre et al. 2019; De Barros et al. 2020). It is true that aseismic slip can lead to smaller values of stress drop as found on fluid-induced earthquakes (e.g., Huang et al. 2019; Jeong et al. 2024). However, Nishimura et al. (2023) demonstrated that the observed crustal deformation during our study period is best modeled by a tensile fault and a shear-tensile fault located in an aseismic area between cluster S and the other clusters.

They suggested that overpressurized fluid ruptured an impermeable seal at a depth of ~ 16 km beneath cluster S, causing aseismic fault movements, and it spread in the permeable shallow-dipping fault zone. Therefore, the northern Noto Peninsula earthquake swarm, especially in clusters W, N, and E, could not have been caused solely by the propagation of aseismic slip to the source areas of these clusters. We, thus, consider that smaller stress drops in the medial part in this study are likely to be caused by the decrease of shear strength associated with the increase of pore pressure, rather than effects of aseismic slip.

As suggested by Yamada et al. (2015), we infer that near the front of hypocenter migration (i.e., in the vicinity of the fluid migration front) the strengths of the source faults decreased only slightly. In contrast, within the faults, where fluids had already penetrated, pore fluid pressure should have already risen, reducing fault strength. As a result, earthquakes with small static stress drops were more likely to occur at medial depths along the source faults, whereas earthquakes with large static stress drops tended to occur at shallow depths along the source faults.

On the other hand, Huang et al. (2017) analyzed induced earthquakes in Oklahoma (USA) and found that the static stress drops of the induced earthquakes were much larger than the pore pressure changes, which were on the order of 10^{-1} MPa (Keranen et al. 2014). According to the slip-weakening friction law, the stress drop is given by $\Delta\sigma = (\mu_s - \mu_d) \times (\sigma_n - P)$, where μ_s is the static friction coefficient, μ_d is the dynamic friction coefficient, σ_n is the normal stress, and P is the pore fluid pressure. For the source area of the earthquake swarm in the northeastern Noto Peninsula, the pore fluid pressure at depths of 11–13 km is estimated to be 250–300 MPa (Ameazawa et al., 2023). Given $\mu_s = 0.6$ and $\mu_d = 0.1$, the observed difference in static stress drops, reaching up to tens of MPa, between the shallow and medial parts is likely attributable to an approximately 10% difference in pore fluid pressure between the two parts.

3.5 A brief discussion of the temporal variation of static stress drops

Previous research on static stress drops in earthquake swarm have reported smaller static stress drops during the early stages of earthquake swarm activity. For example, Yoshida et al. (2019) observed a decrease in static stress drop during the initial stage of earthquake swarm activity due to fluid diffusion along multiple fault planes, enhanced by the east–west extension resulting from the 2011 Tohoku-Oki earthquake. The rise in pore fluid pressure, induced by fluid intrusion into the faults, accounted for the occurrence of earthquakes with smaller static stress drops. However, owing to the absence of earthquakes of magnitude ≥ 3 in the early stages of earthquake swarm activity, we were unable to observe such distinctive temporal variations, whether for the entire swarm or for each cluster (Additional file 1; Figs. S15 and S16).

4 Conclusions

We estimated the corner frequencies of 90 M_{JMA} 3.0–5.4 earthquakes of the northern Noto Peninsula earthquake swarm by using the empirical Green's function method and determined the static stress drop associated with each event. This swarm is known to have been driven by fluid migration. The static stress drops we obtained are consistent with the widely accepted proportional relationship between seismic moment and the inverse of the cube of the corner frequency. We obtained logarithmic mean static stress drops of 13 MPa and 19 MPa based on P-wave and S-wave analyses, respectively, which are typical values for crustal earthquakes. Owing to the relatively small magnitudes of earthquakes in the early stages of the swarm, systematic temporal variations of static stress drops were not readily discernible. Although the spatial distribution of the static stress drops was heterogeneous, clear differences between clusters could not be conclusively identified. In cluster N, however, where more earthquakes occurred and complex fault structures are distinctly observable, we investigated the relationship between hypocenter locations and static stress drops for source faults in different time windows. Our results revealed a tendency for shallow earthquakes along the source faults to have larger static stress drops, whereas earthquakes at medial parts along the source faults had smaller static stress drops. We attribute the large static stress drops at shallow parts to locally high fault strength due to limited fluid diffusion and relatively low pore fluid pressure. Conversely, the small static stress drops at medial parts reflect locally low fault strengths due to high pore fluid pressure after the faults had been penetrated by migrating fluids.

Abbreviations

EGF	Empirical Green's function
JMA	Japan Meteorological Agency
NIED	National Research Institute for Earth Science and Disaster Resilience
S/N	Signal-to-noise ratio

Supplementary Information

The online version contains supplementary material available at https://doi.org/10.1186/s40623-024-02074-9.

Additional File 1.

Acknowledgements
We thank the National Research Institute for Earth Science and Disaster Resilience, the Japan Meteorological Agency, Tokyo University, and Kyoto University, for allowing us to use seismic data. Constructive comments from Yihe Huang and an anonymous reviewer are helpful to improve the manuscript. This work was partly supported by the Japan Society for the Promotion of Science KAKENHI (Grant Numbers JP22K19949 and JP23K17482). All figures were made using GMT software (Wessel et al. 2019).

Author contributions
All authors contributed to the design of this study. MF and YH conducted the analyses. All authors contributed to drafting the manuscript and read and approved the final manuscript.

Funding
This work was partly supported by JSPS KAKENHI (Grant Numbers JP22K19949 and JP23K17482).

Availability of data and materials
Arrival times reported by JMA, seismic moments determined by F-net, NIED, and seismic waveform data from Hi-net and the other institutions can be downloaded from the corresponding websites: (https://www.data.jma.go.jp/eqev/data/bulletin/index_e.html, https://www.fnet.bosai.go.jp/event/search.php?LANG=en, https://hinetwww11.bosai.go.jp/auth/?LANG=en). The relocated hypocenter data are available from YH upon reasonable request.

Declarations

Ethics approval and consent to participate
Not applicable.

Consent for publication
Not applicable.

Competing interests
The authors declare no competing interests.

Author details
[1]Graduate School of Natural Science and Technology, Kanazawa University, Kanazawa 920-1192, Japan. [2]Faculty of Geosciences and Civil Engineering, Institute of Science and Engineering, Kanazawa University, Kanazawa 920-1192, Japan. [3]Faculty of Basic Natural Science, Ibaraki, University, Ibaraki 310-8512, Japan.

Received: 1 April 2024 Accepted: 20 September 2024
Published online: 29 September 2024

References

Abercrombie RE (1995) Earthquake source scaling relationships from −1 to 5. J Geophys Res. https://doi.org/10.1029/95JB02397
Abercrombie RE (2015) Investigating uncertainties in empirical Green's function analysis of earthquake source parameters. J Geophys Res: Solid Earth 120(6):4263–4277. https://doi.org/10.1002/2015JB011984
Allmann BP, Shearer PM (2007) Spatial and temporal stress drop variations in small earthquakes near Parkfield. California J Geophys Res 112:B04305. https://doi.org/10.1029/2006JB004395
Amezawa Y, Hiramatsu Y, Miyakawa A, Imanishi K, Otsubo M (2023) Long-living earthquake swarm and intermittent seismicity in the northeastern tip of the Noto Peninsula Japan. Geophys Res Lett. https://doi.org/10.1029/2022GL102670
Boatwright J (1978) Detailed spectral analysis of two small New York State earthquakes. Bull Seismol Soc Am 68:1131–1177
Brune J (1970) Tectonic stress and the spectra of seismic shear waves from earthquakes. J Geophys Res 75:4997–5009
De Barros L, Cappa F, Deschamps A, Dublanchet P (2020) Imbricated aseismic slip and fluid diffusion drive a seismic swarm in the Corinth Gulf Greece. Geophys Res Lett. https://doi.org/10.1029/2020GL087142
Eyre TS, Eaton DW, Garagash DI, Zecevic M, Venieri M, Weir R, Lawton DC (2019) The role of aseismic slip in hydraulic fracturing–induced seismicity. Sci Adv. https://doi.org/10.1126/sciadv.aav7172
Goertz-Allmann BP, Goertz A, Wiemer S (2011) Stress drop variations of induced earthquakes at the Basel geothermal site. Geophys Res Lett 38:L09308. https://doi.org/10.1029/2011GL047498
Hainzl S, Fischer T, C ermáková H, Bachura M, Vl c ek J, (2016) Aftershocks triggered by fluid intrusion: Evidence for the aftershock sequence occurred 2014 in West Bohemia/Vogtland. J Geophys Res 121:2575–2590. https://doi.org/10.1002/2015JB012582
Hanks TC, Kanamori H (1979) A moment magnitude scale. J Geophys Res 84(B5):2348–2350
Hatch RL, Abercrombie RE, Ruhl CJ, Smith KD (2020) Evidence of aseismic and fluid-driven processes in a small complex seismic swarm near Virginia City Nevada. Geophys Res Lett. https://doi.org/10.1029/2019GL085477
Hayashi M, Hiramatsu Y (2013) Spatial distribution of similar aftershocks of a large inland earthquake, the 2000 Western Tottori earthquake, in Japan. Earth Planets Space 65:1587–1592
Himematsu Y, Furuya M (2015) Aseismic strike–slip associated with the 2007 dike intrusion episode in Tanzania. Tectonophys 656:52–60. https://doi.org/10.1016/j.tecto.2015.06.005
Hiramatsu Y, Yamanaka H, Tadokoro K, Nishigami K, Ohmi S (2002) Scaling law between corner frequency and seismic moment of microearthquakes: Is the breakdown of the cube law a nature of earthquakes? Geophys Res Lett 29(8):1211. https://doi.org/10.1029/2001GL013894
Huang Y, Beroza C, Ellsworth WL (2016) Stress drop estimates of potentially induced earthquakes in the Guy-Greenbrier sequence. J Geophys Res Solid Earth 121:6597–6607. https://doi.org/10.1002/2016JB013067
Huang Y, Ellsworth WL, Beroza GC (2017) Stress drops of induced and tectonic earthquakes in the central United States are indistinguishable. Sci Adv 3(8):e1700772. https://doi.org/10.1126/sciadv.1700772
Huang Y, De Barros L, Cappa F (2019) Illuminating the rupturing of microseismic sources in an injection-induced earthquake experiment. Geophys Res Lett 46:9563–9572. https://doi.org/10.1029/2019GL083856
Imanishi K, Ellsworth WL (2006) Source scaling relationships of microearthquakes at Parkfield, CA, determined using the SAFOD pilot hole seismic array. In: Abercrombie RE, McGarr A, Kanamori H, Di Toro G (eds) Earthquakes: radiated energy and the physics of earthquake faulting, vol 170, Geophys Monogr Ser. AGU, Washington D.C., pp 81–90
Inoue T, Okamura Y (2010) Explanatory notes of 1:200,000 marine geological map around the northern part of Noto Peninsula. Seamless Geoinformation Series of Japanese coastal zones, northern coastal zone of Noto Peninsula, S-1. Bull. Geol. Surv. Jpn. AIST. https://www.gsj.jp/data/coastal-geology/GSJ_DGM_S1_2010_01_b_sim.pdf
Jeong SJ, Tan X, Lui SKY (2024) Fluid-induced aseismic slip may explain the non-self-similar source scaling of the induced earthquake sequence near the Dallas-Fort Worth Airport Texas. J Geophys Res. https://doi.org/10.1029/2023JB027714
Keranen KM, Weingarten M, Abers GA, Bekins BA, Ge S (2014) Sharp increase in central Oklahoma seismicity since 2008 induced by massive wastewater injection. Science 345(6195):448–451. https://doi.org/10.1126/science.1255802
Lengliné O, Lamourette L, Vivin L, Cuenot N, Schmittbuhl J (2014) Fluid-induced earthquakes with variable stress drop. J Geophys Res Solid Earth 119(12):8900–8913. https://doi.org/10.1002/2014JB011282
Madariaga R (1976) Dynamics of an expanding circular fault. Bull Seismol Soc Am 66(3):639–666
Matsubara M, Ishiyama T, No T, Uehira K, Mochizuki M, Kanazawa T, Takahashi N, Kamiya S (2022) Seismic velocity structure along the Sea of Japan with large events derived from seismic tomography for whole Japanese Islands including reflection survey data and NIED MOWLAS Hi-net and S-net data. Earth Planets Space 74:171. https://doi.org/10.1186/s40623-022-01724-0
Nakajima J (2022) Crustal structure beneath earthquake swarm in the Noto peninsula. Japan Earth Planets Space 74:160. https://doi.org/10.1186/s40623-022-01719-x
Nishimura T, Hiramatsu Y, Ohta Y (2023) Episodic transient deformation revealed by the analysis of multiple GNSS networks in the Noto Peninsula, central Japan. Sci Rep 13:8381. https://doi.org/10.1038/s41598-023-35459-z

Okada T, Savage MK, Sakai S, Yoshida K, Uchida N, Takagi R, Kimura S, Hirahara S, Tagami A, Fujimura R, Matsuzawa T, Kurashimo E, Hiramatsu Y (2024) Shear wave splitting and seismic velocity structure in the focal area of the earthquake swarm and their relation with earthquake swarm activity in the Noto Peninsula, central Japan. Earth Planets Space 76:24. https://doi.org/10.1186/s40623-024-01974-0

Oth A (2013) On the characteristics of earthquake stress release variations in Japan. Earth Planet Sci Lett 377–378:132–141. https://doi.org/10.1016/j.epsl.2013.06.037

Ozaki M (2010) 1:200,000 Geological map of the northern part of Noto Peninsula. Seamless Geoinformation Series of Japanese coastal zones, northern coastal zone of Noto Peninsula, S-1. Bull. Geol. Surv. Jpn. AIST. https://www.gsj.jp/data/coastal-geology/GSJ_DGM_S1_2010_02_b.pdf

Ross ZE, Cochran ES (2021) Evidence for latent crustal fluid injection transients in Southern California from long-duration earthquake swarms. Geophys Res Lett. https://doi.org/10.1029/2021GL092465

Ruhl CJ, Abercrombie RE, Smith KD, Zaliapin I (2016) Complex spatiotemporal evolution of the 2008 Mw 49 Mogul earthquake swarm (Reno Nevada): Interplay of fluid and faulting. J Geophys Res. https://doi.org/10.1002/2016JB013399

Shapiro SA, Huenges E, Borm G (1997) Estimating the crust permeability from fluid- injection-induced seismic emission at the KTB site. Geophys J in. https://doi.org/10.1111/j.1365-246X.1997.tb01215.x

Shelly DR, Hill DP, Massin F, Farrell J, Smith RB, Taira T (2013) A fluid-driven earthquake swarm on the margin of the Yellowstone caldera. J Geophys Res 118:4872–4886. https://doi.org/10.1002/jgrb.50362

Takada Y, Furuya M (2010) Aseismic slip during the 1996 earthquake swarm in and around the Onikobe geothermal area, NE Japan. Earth Planet Sci Lett 290:302–310. https://doi.org/10.1016/j.epsl.2009.12.024

Uchide T, Shearer PM, Imanishi K (2014) Stress drop variations among small earthquakes before the 2011 Tohoku-oki, Japan, earthquake and implications for the main shock. J Geophys Res Solid Earth 119:7164–7174. https://doi.org/10.1002/2014JB010943

Ueno H, Hatakeyama S, Aketagawa T, Funasaki J, Hamada N (2002) Improvement of hypocenter determination procedures in the Japan Meteorological Agency. Q J Seismol 65:123–134

Urano S, Hiramatsu Y, Yamada T et al (2015) Relationship between coseismic slip and static stress drop of similar aftershocks of the 2007 Noto Hanto earthquake. Earth Planets Space 67:101. https://doi.org/10.1186/s40623-015-0277-0

Waldhauser F, Ellsworth WL (2000) A double-difference earthquake location algorithm: Method and application to the northern Hayward fault, California. Bull Seismol Soc Am 90:1353–1368. https://doi.org/10.1785/0120000006

Wessel P, Luis JF, Uieda L, Scharroo R, Wobbe F, Smith WHF, Tian D (2019) The generic mapping tools version 6. Geochem Geophys Geosyst. https://doi.org/10.1029/2019GC008515

Yamada T, Okubo PG, Wolfe CJ (2010) Kīholo Bay, Hawai`i, earthquake sequence of 2006: relationship of the main shock slip with locations and source parameters of aftershocks. J Geophys Res 115:B08304. https://doi.org/10.1029/2009JB006657

Yamada T, Yukutake Y, Terakawa T, Arai R (2015) Migration of earthquakes with a small stress drop in the Tanzawa Mountains Japan. Earth Planets Space 67:175. https://doi.org/10.1186/s40623-015-0344-6

Yamada T, Saito Y, Tanioka Y, Kawahara J (2017) Spatial pattern in stress drops of moderate-sized earthquakes on the Pacific Plate off the south-east of Hokkaido, Japan: Implications for the heterogeneity of frictional properties. Prog Earth Planet Sci 4:38. https://doi.org/10.1186/s40645-017-0152-7

Yamada T, Duan M, Kawahara J (2021) Spatio-temporal characteristics of frictional properties on the subducting Pacific Plate off the east of Tohoku district, Japan estimated from stress drops of small earthquakes. Earth Planets Space 73:18. https://doi.org/10.1186/s40623-020-01326-8

Yoshida K, Saito T, Emoto K, Urata Y, Sato D (2019) Rupture directivity, stress drop, and hypocenter migration of small- and moderate-sized earthquakes in the Yamagata-Fukushima border swarm triggered by upward pore-pressure migration after the 2011 Tohoku-Oki earthquake. Tectonophys 769:228184. https://doi.org/10.1016/j.tecto.2019.228184

Yoshida K, Uno M, Matsuzawa T, Yukutake Y, Mukuhira Y, Sato H, Yoshida T (2023) Upward earthquake swarm migration in the northeastern Noto Peninsula, Japan, initiated from a deep ring-shaped cluster: Possibility of fluid leakage from a hidden magma system. J Geophys Res Solid Earth. https://doi.org/10.1029/2022JB026047

Yoshimitsu N, Kawakata H, Takahashi N (2014) Magnitude −7 level earthquakes: a new lower limit of self-similarity in seismic scaling relationships. Geophys Res Lett 41:4495–4502. https://doi.org/10.1002/2014GL060306

Yoshimura R, Hiramatsu Y, Goto T, Kasaya T, Miyamachi R, Jun N, Yamashita N, Amano R, Fukata M, Sugii A, Inui T, Yamazaki K, Komatsu S, Iwahori T, Yoshikawa M, Namigishi A, Nagaoka A, Tatsuyama Y, Sawada A, Zhang C, Fukuoka M, Jinde Y, Oshima Y, Kanazawa M (2023) Three-dimensional resistivity structure around earthquake swarm region in the northeastern Noto Peninsula. Japan Geoscience Union Meeting 2023 SGC56-P08.

Yukutake Y, Yoshida K, Honda R (2022) Interaction between aseismic slip and fluid invasion in earthquake swarms revealed by dense geodetic and seismic observations. J Geophys Res Solid Earth. https://doi.org/10.1029/2021JB022933

Publisher's Note